Density functional theory of graphene sheets

Marco Polini,[1,*] Andrea Tomadin,[1] Reza Asgari,[2] and A. H. MacDonald[3]
[1]*NEST-CNR-INFM and Scuola Normale Superiore, I-56126 Pisa, Italy*
[2]*School of Physics, Institute for Research in Fundamental Sciences, 19395-5531 Tehran, Iran*
[3]*Department of Physics, The University of Texas at Austin, Austin, Texas 78712, USA*
(Received 28 March 2008; revised manuscript received 6 June 2008; published 23 September 2008)

We outline a Kohn-Sham-Dirac density functional theory (DFT) scheme for graphene sheets that treats slowly varying inhomogeneous external potentials and electron-electron interactions on equal footing. The theory is able to account for the unusual property that the exchange-correlation contribution to chemical potential increases with carrier density in graphene. The consequences of this property and advantages and disadvantages of using the DFT approach to describe it are discussed. The approach is illustrated by solving the Kohn-Sham-Dirac equations self-consistently for a model random potential describing charged pointlike impurities located close to the graphene plane. The influence of electron-electron interactions on these nonlinear screening calculations is discussed at length in light of recent experiments reporting evidence for the presence of electron-hole puddles in nearly neutral graphene sheets.

DOI: 10.1103/PhysRevB.78.115426 PACS number(s): 71.15.Mb, 71.10.Ca, 72.10.−d

I. INTRODUCTION

Graphene is a newly realized two-dimensional (2D) electron system,[1,2] which has engendered a great deal of interest because of the new physics which it exhibits and because of its potential as a new material for electronic technology. The agent responsible for many of the interesting electronic properties of graphene sheets is the non-Bravais honeycomb-lattice arrangement of carbon atoms, which leads to a gapless semiconductor with valence and conduction π bands. States near the Fermi energy of a graphene sheet are described by a massless Dirac equation which has chiral band states in which the honeycomb-sublattice pseudospin is aligned either parallel to or opposite to the envelope-function momentum. The Dirac-like wave equation leads to both unusual electron-electron interaction effects and unusual response to external potentials.

Many new ideas that are now being explored in graphene electronics are still based on idealized models which neglect disorder and electron-electron interactions. As a consequence many of these may ultimately require qualitative and quantitative revision as our understanding of this material improves. In this paper we outline one approach, which we term as "Kohn-Sham (KS) -Dirac DFT,"[3] that can be used for more realistic modeling of graphene sheets, including both disorder and electron-electron interactions.

Because of band chirality, the role of electron-electron interactions in graphene sheets differs in some essential ways[4–6] from the role which it plays in an ordinary 2D electron gas. One important difference is that the contribution of exchange and correlation to the chemical potential is an increasing rather than a decreasing function of carrier density. As we will discuss later, this property implies that exchange and correlation increase the effectiveness of screening, in contrast to the usual case in which exchange and correlation weaken screening. This unusual property follows from the difference in sublattice-pseudospin chirality between the Dirac model's negative-energy valence-band states and its conduction-band states,[4,5] and in a uniform graphene system is readily accounted for by many-body perturbation theory. The principle merit of the DFT theory we describe is that it allows this physics to be accounted for in graphene sheets in which the carrier density is nonuniform either by design, as in *p-n* junction systems,[7] or as a result of unintended disorder sources.

A related and complementary DFT method was recently used by Rossi and Das Sarma[8] to study the ground-state density profile of massless Dirac fermions in the presence of randomly distributed charged impurities. Their method differs from ours in two main respects: The authors of Ref. 8 (i) approximated the kinetic-energy functional of noninteracting massless Dirac fermions by means of a local-density approximation (LDA), whereas in the present work the kinetic-energy functional is treated exactly via the Kohn-Sham mapping (see Sec. II below); and (ii) neglected correlation effects, which, as it will be clear in Sec. II B, partly compensate for the enhanced screening due to exchange and Dirac-equation chirality. Inhomogeneous graphene systems were also studied using the Thomas-Fermi approximation (LDA for the kinetic energy only) by Fogler and co-workers.[9]

Our paper is organized as follows: In Sec. II we outline the version of DFT which is appropriate for nonuniform carrier-density graphene sheets with static external potentials that are smooth enough to permit neglect of intervalley scattering. Many-body effects enter this theory via an LDA exchange-correlation potential with a density dependence precisely opposite to the one familiar from ordinary LDA-DFT theory applied to parabolic-band inhomogeneous electron liquids. In Sec. III we outline the procedure we have used to solve the theory's Dirac-like Kohn-Sham equations. In Sec. IV we discuss results obtained by solving the Kohn-Sham equations self-consistently for an illustrative random potential model, highlighting some strengths and weaknesses of this approach to many-body physics in inhomogeneous graphene sheets. In Sec. V we briefly mention other problems to which the theory outlined in this paper could be successfully applied and comment on the relationship between our DFT approach and *ab initio* DFT applied to

 ©2008 The American Physical Society

graphene. Finally, in Sec. VI we summarize our main conclusions.

II. MASSLESS DIRAC-MODEL DFT

We consider a system of 2D massless Dirac fermions which are subjected to a time-independent scalar external potential $V_{\rm ext}(\boldsymbol{r})$. This model applies to graphene sheets when the external potential varies slowly on the lattice-constant length scale. In this limit the external potential will couple identically to the two sublattices and is hence a pseudospin scalar and has negligible intervalley scattering, justifying an envelope-function approach,[10] which promotes the perfect crystal Dirac bands to envelope-function Dirac operators. To account for electron-electron interactions in graphene sheets, the ultrarelativistic massless Dirac particles must interact via instantaneous nonrelativistic Coulomb interactions. The juxtaposition of an ultrarelativistic free-fermion term and a nonrelativistic interaction term in the Hamiltonian of a graphene sheet leads to a new type of many-body problem.

DFT (Refs. 11–13) is a practical approach to many-body physics which recognizes the impossibility of achieving exact results and seeks practical solutions with adequate accuracy. Following a familiar line of argument[11–13] which we do not reproduce here, many-body exchange-correlation effects can be taken into account in the graphene many-body problem with the same formal justifications and the same types of approximation schemes as in standard nonrelativistic DFT.[11–13] The end result in the case of present interest is that ground-state charge densities and energies are determined by solving a time-independent Kohn-Sham-Dirac equation for a sublattice-pseudospin spinor $\Phi_\lambda(\boldsymbol{r})=[\varphi_\lambda^{(A)}(\boldsymbol{r}),\varphi_\lambda^{(B)}(\boldsymbol{r})]^T$,

$$[v\boldsymbol{\sigma}\cdot\boldsymbol{p}+\mathbb{I}_\sigma V_{\rm KS}(\boldsymbol{r})]\Phi_\lambda(\boldsymbol{r})=\varepsilon_\lambda\Phi_\lambda(\boldsymbol{r}). \tag{1}$$

Here $v\sim 10^6$ m/s is the bare Fermi velocity, $\boldsymbol{p}=-i\hbar\nabla_{\boldsymbol{r}}$, $\boldsymbol{\sigma}$ is a 2D vector constructed with the 2×2 Pauli matrices σ_1 and σ_2 acting in pseudospin space, $\mathbb{I}_\sigma$ is the 2×2 identity matrix in pseudospin space, and $V_{\rm KS}(\boldsymbol{r})=V_{\rm ext}(\boldsymbol{r})+\Delta V_H(\boldsymbol{r})+V_{\rm xc}(\boldsymbol{r})$ is the Kohn-Sham potential, which is a functional of the ground-state density $n(\boldsymbol{r})$. The ground-state density is obtained as a sum over occupied Kohn-Sham-Dirac spinors $\Phi_\lambda(\boldsymbol{r})$:

$$n(\boldsymbol{r})=4\sum_{\lambda({\rm occ})}\Phi_\lambda^\dagger(\boldsymbol{r})\Phi_\lambda(\boldsymbol{r})\equiv 4\sum_{\lambda({\rm occ})}[|\varphi_\lambda^{(A)}(\boldsymbol{r})|^2+|\varphi_\lambda^{(B)}(\boldsymbol{r})|^2], \tag{2}$$

where the factor 4 is due to valley and spin degeneracies and $\{\varphi_\lambda^{(\sigma)}(\boldsymbol{r}),\sigma=A,B\}$ are the pseudospin (sublattice) components of the Kohn-Sham-Dirac spinor $\Phi_\lambda(\boldsymbol{r})$. Equation (2) is a self-consistent closure relationship for Kohn-Sham-Dirac equation (1), since the effective potential in Eq. (1) is a functional of the ground-state density $n(\boldsymbol{r})$. More explicit details on the construction of $n(\boldsymbol{r})$ are given below. This formalism is readily generalized to account for spin polarization,[14] or valley polarization,[15] or both. A generalization of the present theory to situations in which graphene is subjected to an inhomogeneous magnetic field (as in magnetically defined graphene quantum dots[16]) can also be envisioned along the lines of, e.g., Ref. 17.

The KS potential $V_{\rm KS}(\boldsymbol{r})$ in Eq. (1) is the sum of external, Hartree, and exchange-correlation contributions. The Hartree potential

$$\Delta V_H(\boldsymbol{r})=\int d^2\boldsymbol{r}'\frac{e^2}{\epsilon|\boldsymbol{r}-\boldsymbol{r}'|}\delta n(\boldsymbol{r}'), \tag{3}$$

where ϵ is the average background dielectric constant ($\epsilon=2.5$, for example, for graphene placed on SiO_2 with the other side exposed to air) and the quantity $\delta n(\boldsymbol{r})=n(\boldsymbol{r})-n_0$ is the density measured relative to that of a uniform neutral graphene sheet as specified more precisely below [see Eq. (34)].

The third term in $V_{\rm KS}(\boldsymbol{r})$, $V_{\rm xc}(\boldsymbol{r})$, is the exchange-correlation potential, which is formally a functional of the ground-state density but known only approximately. In this work we employ the local-density approximation,

$$V_{\rm xc}(\boldsymbol{r})=v_{\rm xc}^{\rm hom}(n)|_{n\to n_c(\boldsymbol{r})}, \tag{4}$$

where $v_{\rm xc}^{\rm hom}(n)$ is the reference exchange-correlation potential of a *uniform 2D liquid of massless Dirac fermions*[4,5] with carrier density n. $v_{\rm xc}^{\rm hom}(n)$ is related to the ground-state energy per excess carrier $\delta\varepsilon_{\rm xc}(n)$ as

$$v_{\rm xc}^{\rm hom}(n)=\frac{\partial[n\,\delta\varepsilon_{\rm xc}(n)]}{\partial n}. \tag{5}$$

The carrier density $n_c(\boldsymbol{r})$ is the density relative to that of a uniform *neutral* graphene sheet and will be defined more precisely in Sec. IV A. The expression used for $\delta\varepsilon_{\rm xc}(n)$ depends on the zero of energy, which is normally[4,5] chosen so that $v_{\rm xc}^{\rm hom}(n=0)=0$.

To apply the LDA-DFT formalism to graphene, it is necessary to have convenient expressions for the excess exchange-correlation energy $\delta\varepsilon_{\rm xc}(n)$, which will be provided below in Secs. II A and II B. This quantity was calculated at the random-phase-approximation (RPA) level in Ref. 4.

A. Exchange potential

Because the Coulomb energy and the Dirac band energy scale in the same way with length, we can write the first-order exchange contribution to $\delta\varepsilon_{\rm xc}(n)$ as

$$\delta\varepsilon_x(n)=\varepsilon_F\alpha_{\rm gr}F(\Lambda). \tag{6}$$

Here $\varepsilon_F={\rm sgn}(n)\hbar vk_F$ is the Fermi energy, where $k_F=(4\pi|n|/g)^{1/2}$ is the Fermi wave vector corresponding to an electron (hole) density n above (below) the neutrality point and $g=g_sg_v=4$ accounts for spin and valley degeneracies. The quantity $\alpha_{\rm gr}$ is defined as $\alpha_{\rm gr}=ge^2/(\epsilon\hbar v)\equiv g\alpha_{\rm ee}$, where $\alpha_{\rm ee}$ is graphene's fine structure constant. The ultraviolet cutoff Λ in Eq. (6) is defined as $\Lambda=k_{\rm max}/k_F$, where $k_{\rm max}$ should be assigned a value corresponding to the wave-vector range over which the continuum model describes graphene. For definiteness we take $k_{\rm max}$ to be such that

$$\pi k_{\rm max}^2=\eta\frac{(2\pi)^2}{\mathcal{A}_0}, \tag{7}$$

where $\mathcal{A}_0=3\sqrt{3}a_0^2/2\sim 0.052$ nm^2 is the area of the unit cell in the honeycomb lattice ($a_0\simeq 1.42$ Å is the carbon-carbon

distance) and η is a dimensionless number $\eta \in (0,1]$. The optimal value of η would have to be determined by a lattice-model correlation energy calculation. From another point of view η, the Dirac velocity v, and the dielectric constant ϵ are coupled parameters of the Dirac model for graphene which should be fixed by comparison of the model's predictions with experiment. For typical graphene-system densities, the dependence of the exchange-correlation potential on η is weak enough that we can arbitrarily choose $\eta=1$ with some confidence. Given a value of η, the dependence of Λ on density is given by

$$\Lambda(n) = \sqrt{g\eta}\frac{1}{\sqrt{|n|\mathcal{A}_0}}. \tag{8}$$

The exchange potential corresponding to Eq. (6) is given by

$$v_x^{\mathrm{hom}}(n) \equiv \frac{\partial[n\,\delta\varepsilon_x(n)]}{\partial n} = \frac{3}{2}\varepsilon_F\alpha_{\mathrm{gr}}F(\Lambda) + \varepsilon_F\alpha_{\mathrm{gr}}\frac{\partial F}{\partial\Lambda}n\frac{\partial\Lambda}{\partial n}, \tag{9}$$

where

$$n\frac{\partial\Lambda}{\partial n} = -\frac{1}{2}\Lambda. \tag{10}$$

We have chosen the following simple formula for $F(\Lambda)$ to parametrize the data in Ref. 4:

$$F(\Lambda) = \frac{1}{6g}\ln(\Lambda) + \frac{a_e}{1+b_e\Lambda^{c_e}}, \tag{11}$$

where the first term, which is the leading contribution in the limit $\Lambda \gg 1$, was calculated analytically in Ref. 4. This term is largely responsible for the quasiparticle velocity enhancement in doped graphene sheets.[4,5] The numerical constants a_e, b_e, and c_e are given by

$$a_e = 0.017\,3671,$$

$$b_e = 3.6642 \times 10^{-7},$$

$$c_e = 1.6784. \tag{12}$$

Equation (11) implies that

$$\frac{\partial F}{\partial\Lambda} = -\frac{a_e b_e c_e}{(1+b_e\Lambda^{c_e})^2}\frac{\Lambda^{c_e}}{\Lambda} + \frac{1}{6g}\frac{1}{\Lambda}. \tag{13}$$

Note that for $n\to 0$ the exchange potential goes to zero such as

$$v_x^{\mathrm{hom}}(n\to 0) \propto -\,\mathrm{sgn}(n)\alpha_{\mathrm{gr}}\sqrt{|n|}\ln|n|, \tag{14}$$

i.e., with an infinite slope.

B. RPA correlation potential

The RPA correlation energy data of Ref. 4 can be conveniently parametrized by the following formula:

$$\frac{\delta\varepsilon_c^{\mathrm{RPA}}(n)}{\varepsilon_F} = -\frac{\alpha_{\mathrm{gr}}^2}{6g}\xi(\alpha_{\mathrm{gr}})\ln(\Lambda) + \frac{\alpha_{\mathrm{gr}}^2 a_c(\alpha_{\mathrm{gr}})}{1+b_c(\alpha_{\mathrm{gr}})\Lambda^{c_c(\alpha_{\mathrm{gr}})}}, \tag{15}$$

where

$$a_c(\alpha_{\mathrm{gr}}) = -\,1/(63.0963 + 57.351\,226\alpha_{\mathrm{gr}}),$$

$$b_c(\alpha_{\mathrm{gr}}) = (7.750\,95 - 0.083\,71\alpha_{\mathrm{gr}}^{1.611\,67}) \times 10^{-7},$$

$$c_c(\alpha_{\mathrm{gr}}) = 1.527 + 0.0239\alpha_{\mathrm{gr}} - 0.001\,201\alpha_{\mathrm{gr}}^2, \tag{16}$$

and

$$\xi(\alpha_{\mathrm{gr}}) = \frac{1}{2}\int_0^{+\infty}\frac{dx}{(1+x^2)^2(\sqrt{1+x^2}+\pi\alpha_{\mathrm{gr}}/8)}. \tag{17}$$

Once again, the logarithmic contribution in Eq. (15) represents the leading term in the limit $\Lambda \gg 1$ and was calculated analytically in Ref. 4.

Note that we can write Eq. (15) in the form

$$\delta\varepsilon_c^{\mathrm{RPA}} = \varepsilon_F\alpha_{\mathrm{gr}}^2 G_{\alpha_{\mathrm{gr}}}(\Lambda), \tag{18}$$

with

$$G_{\alpha_{\mathrm{gr}}}(\Lambda) = -\frac{\xi(\alpha_{\mathrm{gr}})}{6g}\ln(\Lambda) + \frac{a_c(\alpha_{\mathrm{gr}})}{1+b_e(\alpha_{\mathrm{gr}})\Lambda^{c_e(\alpha_{\mathrm{gr}})}}. \tag{19}$$

Following the same procedure highlighted above for the exchange contribution, one easily finds the correlation contribution to $v_{\mathrm{xc}}^{\mathrm{hom}}(n)$. The only necessary input to calculate this contribution is

$$\frac{\partial G_{\alpha_{\mathrm{gr}}}}{\partial\Lambda} = -\frac{a_c b_c c_c}{(1+b_c\Lambda^{c_c})^2}\frac{\Lambda^{c_c}}{\Lambda} - \frac{\xi(\alpha_{\mathrm{gr}})}{6g}\frac{1}{\Lambda}. \tag{20}$$

In the limit $n\to 0$ we find

$$v_c^{\mathrm{hom}}(n\to 0) \propto \mathrm{sgn}(n)\alpha_{\mathrm{gr}}^2\xi(\alpha_{\mathrm{gr}})\sqrt{|n|}\ln|n|. \tag{21}$$

A plot of the exchange-correlation potential as a function of the density n is given in Fig. 1. For the sake of comparison, in Fig. 1 we also have plotted the quantum Monte Carlo exchange-correlation potential of the parabolic-band 2D electron gas,[18] after having antisymmetrized it for $n<0$. We can clearly see from this plot how the density dependence of the exchange-correlation potential of a uniform 2D liquid of massless Dirac fermions is precisely opposite to the one familiar from the ordinary LDA for parabolic-band inhomogeneous electron liquids. While the latter is negative for positive density, favoring inhomogeneous densities, the former increases the energy cost of density increases, favoring more homogeneous densities and enhancing screening. It is also apparent from this figure that the density dependence of the exchange-correlation potential can in some circumstances lead to effects which can give the appearance of a gap in the graphene sheet's Dirac bands.

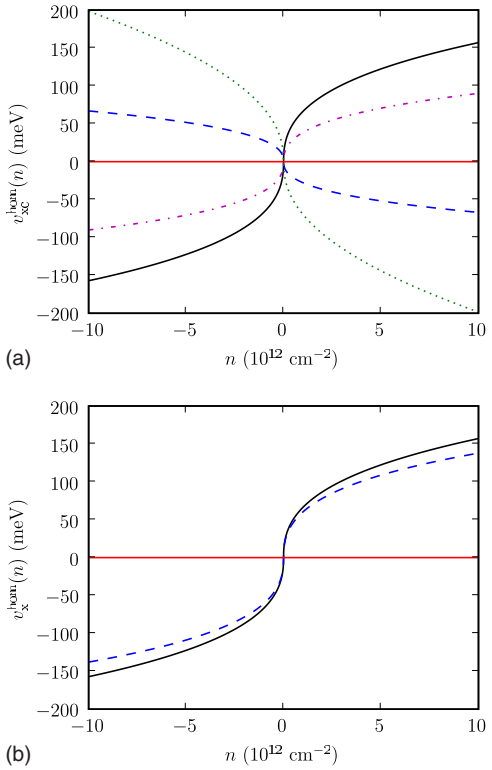

FIG. 1. (Color online) Top panel: The exchange and RPA correlation potentials, $v_x^{\rm hom}(n)$ [(black) solid line] and $v_c^{\rm hom}(n)$ [(blue) dashed line] (in meV), as functions of the density n (in units of 10^{12} cm^{-2}) for $\alpha_{\rm ee}=0.5$. Note how for $n\to 0$ both potentials have an infinite slope. The (magenta) dash-dotted line represents the full exchange-correlation potential, $v_{\rm xc}^{\rm hom}(n)=v_x^{\rm hom}(n)+v_c^{\rm hom}(n)$. The (green) dotted line is the quantum Monte Carlo exchange-correlation potential of a standard parabolic-band 2D electron gas (Ref. 18). For convenience we have chosen parameters corresponding to a 2D electron gas on a background with dielectric constant of 4 and with band mass of $0.067m$, m being the electron mass in vacuum. Bottom panel: The full exchange potential [(black) solid line] is compared with its natural-logarithm-only approximation, [(blue) dashed line], i.e., retaining only the first term in Eq. (11).

III. KOHN-SHAM-DIRAC EQUATION SOLUTIONS: PLANE-WAVE METHOD

In this section we discuss Kohn-Sham-Dirac equation solutions based on a supercell method and plane-wave expansions. We consider massless Dirac fermions in a 2D (square) box of size $L\times L$ with *periodic* boundary conditions. In this case Kohn-Sham-Dirac equation (1) can be conveniently solved by expanding the spinors $\Phi_\lambda(\boldsymbol{r})$ in a plane-wave basis. We discretize real space: $\boldsymbol{r}\to\boldsymbol{r}_{ij}=(x_i,y_j)$, $x_i=i\delta x$, and $y_j=j\delta y$, with $i=1,\ldots,N_x$ and $j=1,\ldots,N_y$. Here $\delta x\times N_x=\delta y\times N_y=L$. Fourier transforms $\tilde{f}(\boldsymbol{k})$ of real-space functions $f(\boldsymbol{r})$ are calculated by means of a standard fast-Fourier-transform algorithm[19] that allows us to compute $\tilde{f}$ on the set of discrete wave vectors $\boldsymbol{k}_{ij}$,

$$\boldsymbol{k}_{ij}=(k_{x,i},k_{y,j})=\frac{2\pi}{L}(n_{x,i},n_{y,j}), \tag{22}$$

with $-N_x/2\le n_{x,i}<N_x/2$ and $-N_y/2\le n_{y,j}<N_y/2$ (or, equivalently, $0\le n_{x,i}<N_x$ and $0\le n_{y,j}<N_y$), that belong to the Bravais lattice of the discretized box. The definition of the Fourier transform that we use is the following:

$$f(\boldsymbol{r})=\int\frac{d^2\boldsymbol{k}}{(2\pi)^2}\tilde{f}(\boldsymbol{k})e^{i\boldsymbol{k}\cdot\boldsymbol{r}},$$

$$\tilde{f}(\boldsymbol{k})=\int d^2\boldsymbol{r}f(\boldsymbol{r})e^{-i\boldsymbol{k}\cdot\boldsymbol{r}}. \tag{23}$$

After discretization $f(\boldsymbol{r})\to f_{ij}=f(\boldsymbol{r}_{ij})$, $\tilde{f}_{ij}=\tilde{f}(\boldsymbol{k}_{ij})$, with

$$f_{ij}=\frac{1}{L^2}\sum_{n=0}^{N_x-1}\sum_{m=0}^{N_y-1}\tilde{f}_{nm}e^{i\boldsymbol{k}_{nm}\cdot\boldsymbol{r}_{ij}} \tag{24}$$

and

$$\tilde{f}_{ij}=L^2\frac{1}{N_xN_y}\sum_{n=0}^{N_x-1}\sum_{m=0}^{N_y-1}f_{nm}e^{-i\boldsymbol{k}_{ij}\cdot\boldsymbol{r}_{nm}}. \tag{25}$$

In all the numerical calculations reported on below, we use L as the unit of length, $2\pi\hbar/L$ as the unit of momentum, and $\hbar v/L$ as the unit of energy. In what follows we also set $\hbar=1$.

In momentum space Eq. (1) reads

$$\sum_{\boldsymbol{k}'}\langle\boldsymbol{k}|[v\boldsymbol{\sigma}\cdot\boldsymbol{p}+\mathbb{I}_\sigma V_{\rm KS}(\boldsymbol{r})]|\boldsymbol{k}'\rangle\tilde{\Phi}_\lambda(\boldsymbol{k}')=\varepsilon_\lambda\tilde{\Phi}_\lambda(\boldsymbol{k}). \tag{26}$$

Here λ labels the eigenvalues of the Kohn-Sham-Dirac matrix $\mathcal{H}^{\rm KSD}_{\boldsymbol{k},\boldsymbol{k}'}\equiv\langle\boldsymbol{k}|[v\boldsymbol{\sigma}\cdot\boldsymbol{p}+\mathbb{I}_\sigma V_{\rm KS}(\boldsymbol{r})]|\boldsymbol{k}'\rangle$. The matrix elements of the kinetic Hamiltonian are given by

$$\langle\boldsymbol{k}|v\boldsymbol{\sigma}\cdot\boldsymbol{p}|\boldsymbol{k}'\rangle=v\boldsymbol{\sigma}\cdot\boldsymbol{k}'\,\delta_{\boldsymbol{k},\boldsymbol{k}'}. \tag{27}$$

We employ a momentum-space cutoff $k_{x,i},k_{y,j}\in[-k_c,+k_c]$ which does not exceed the Brillouin-zone boundary defined by our real-space discretization: $k_c<\pi/\delta x,\pi/\delta y$. k_c defines the range of momenta used in the expansion of the Hamiltonian $\mathcal{H}^{\rm KSD}_{\boldsymbol{k},\boldsymbol{k}'}$ and thus defines its dimension d_H as

$$d_H=2\left(2\frac{Lk_c}{2\pi}+1\right)^2. \tag{28}$$

The factor of 2 here is due to the sublattice-pseudospin degree of freedom. As already stated above, real spin and valley degrees of freedom enter our calculations only through the trivial degeneracy factors they imply. Given a value of k_c the Kohn-Sham-Dirac matrix $\mathcal{H}^{\rm KSD}_{\boldsymbol{k},\boldsymbol{k}'}$ has d_H eigenvalues, labeled by the discrete index $\lambda=1,\ldots,d_H$.

IV. NONLINEAR SCREENING OF COULOMB IMPURITIES

As an illustration we apply the LDA-DFT method described above to study the nonlinear screening of $N_{\rm imp}\ge 1$ pointlike impurities with charge Ze (Z can be either positive or negative and $e>0$ in this work) located at random positions on a plane at a distance d from the 2D chiral electron gas (CEG) plane. The approximately linear dependence of conductivity on carrier density in graphene sheets

suggests[20,21] that nearby charged impurities are the dominant disorder source in most current graphene samples.

A. Constructing the KS potential and the ground-state density

We assume that the 2D CEG has a spatially averaged π-electron density

$$n_0 = \frac{2}{\mathcal{A}_0} + \bar{n}_c. \tag{29}$$

Here $2/\mathcal{A}_0$ is the density of a neutral graphene sheet and $\bar{n}_c$ is the spatially averaged carrier density, which can be positive or negative and controlled by gate voltages.[1,22,23] In what follows we write $\bar{n}_c \equiv 4\mathcal{Q}/L^2$, where $\mathcal{Q}$ is the number of carriers per spin and valley in our supercell. Because of the role played by gate voltages in experiment, there is no reason to impose a charge-neutrality relationship between the number of impurities $N_{\rm imp}$ and $\mathcal{Q}$.

The external potential $V_{\rm ext}(\boldsymbol{r})$ is given by

$$V_{\rm ext}(\boldsymbol{r}) = -\sum_{i=1}^{N_{\rm imp}} \frac{Ze^2}{\epsilon\sqrt{|\boldsymbol{r}-\boldsymbol{R}_i|^2 + d^2}}, \tag{30}$$

where $\boldsymbol{R}_i$ are random positions in the supercell. For simplicity, all charges have been taken to have the same Z in Eq. (30) (cf. Ref. 24). The matrix elements of the disorder potential in Eq. (30) are given by

$$\langle \boldsymbol{k}|V_{\rm ext}(\boldsymbol{r})|\boldsymbol{k}'\rangle = \tilde{V}_{\rm ext}(\boldsymbol{k}-\boldsymbol{k}')\mathcal{F}_{\rm imp}(\boldsymbol{k}-\boldsymbol{k}'), \tag{31}$$

where $\tilde{V}_{\rm ext}(\boldsymbol{q}) = -2\pi Ze^2 \exp(-qd)/(\epsilon q)$ is the Fourier transform of the potential created by a single impurity and

$$\mathcal{F}_{\rm imp}(\boldsymbol{k}-\boldsymbol{k}') = \frac{1}{L^2}\sum_{i=1}^{N_{\rm imp}} e^{-i(\boldsymbol{k}-\boldsymbol{k}')\cdot\boldsymbol{R}_i} \tag{32}$$

is a geometric form factor that depends only on the positions of the impurities. The impurity charges are replicated in each supercell and the total potential $V_{\rm ext}(\boldsymbol{r})$ therefore has the supercell periodicity. We set $\tilde{V}_{\rm ext}(\boldsymbol{k}=\boldsymbol{k}')=0$, thereby choosing the zero of energy at the Dirac-point energy in the spatially averaged external potential.

The ground-state density profile $n(\boldsymbol{r})$ in the external potential given by Eq. (30) is computed from Eq. (2) by summing over $\lambda = 1, \ldots, \lambda_{\rm max}$, where the KS energy levels are arranged in ascending order, $\varepsilon_1 \le \cdots \le \varepsilon_{\lambda_{\rm max}} \le \cdots \le \varepsilon_{d_H}$. Since half of the system's π orbitals are occupied in a neutral graphene sheet, $\lambda_{\rm max}$ is related to the average π-electron density of the graphene sheet $n_0 = 4(d_H/2 + \mathcal{Q})/L^2$ by

$$\lambda_{\rm max} = \frac{d_H}{2} + \mathcal{Q}. \tag{33}$$

Note that this implies the following relationship between the momentum-space cutoff k_c and the area of the system L^2 in units of $\mathcal{A}_0$: $L^2/\mathcal{A}_0 = 2[2Lk_c/(2\pi)+1]^2$. In our self-consistent numerical calculations, we evaluate only the deviation of the density from its average value in the supercell:

$$\delta n(\boldsymbol{r}) = n(\boldsymbol{r}) - n_0. \tag{34}$$

The corresponding quantity in momentum space $\delta\tilde{n}(\boldsymbol{k})$ is given by $\delta\tilde{n}(\boldsymbol{k}) = \tilde{n}(\boldsymbol{k}) - n_0\delta_{\boldsymbol{k},0}$. Note that $\delta n(\boldsymbol{r})$ is *charge neutral*, i.e., $\delta\tilde{n}(\boldsymbol{k}=0)=0$. The matrix elements of the Hartree term in the Kohn-Sham-Dirac equation are given by

$$\langle \boldsymbol{k}|\Delta V_H(\boldsymbol{r})|\boldsymbol{k}'\rangle = \frac{2\pi e^2}{\epsilon|\boldsymbol{k}-\boldsymbol{k}'|}\delta\tilde{n}(\boldsymbol{k}-\boldsymbol{k}'). \tag{35}$$

The matrix elements of the exchange-correlation potential can be calculated numerically from

$$\langle \boldsymbol{k}|V_{\rm xc}(\boldsymbol{r})|\boldsymbol{k}'\rangle = \frac{1}{L^2}\int d^2\boldsymbol{r} V_{\rm xc}(\boldsymbol{r}) e^{-i(\boldsymbol{k}-\boldsymbol{k}')\cdot\boldsymbol{r}}, \tag{36}$$

where $V_{\rm xc}(\boldsymbol{r})$ is given by Eq. (4) with the carrier density

$$n_c(\boldsymbol{r}) = n(\boldsymbol{r}) - \frac{2d_H}{L^2} = \delta n(\boldsymbol{r}) + \frac{4\mathcal{Q}}{L^2}. \tag{37}$$

B. Numerical results

In this section we report some illustrative numerical results that we have obtained by applying the LDA-DFT method described above. All the numerical results presented in this work were obtained with $\eta=1$ [see Eq. (7) for the definition of η].

In Fig. 2 we illustrate the real-space density profile $\delta n(\boldsymbol{r})$ of a neutral-on-average ($\mathcal{Q}=0$) 2D CEG subjected to the external potential of $N_{\rm imp}=40$ impurities with $Z=+1$ located at a distance $d=0.1L$ from the graphene plane. [The corresponding external potential $V_{\rm ext}(\boldsymbol{r})$ is illustrated in the top left panel of Fig. 2.] In this particular simulation we have used $\alpha_{\rm ee}=0.5$ and $k_c=(2\pi/L)10$, which corresponds to an effective square size $L^2 = 882\mathcal{A}_0 \sim 46$ nm^2. The charges are therefore separated from the graphene layer by $d \sim 0.7$ nm. This model is motivated by growing experimental evidence that the dominant source of disorder in most graphene samples is external charges, probably located in the nearby substrate.

In Fig. 2 we have reported: (i) the non-interacting Dirac electron-density profile, which is obtained by setting the Hartree and exchange-correlation potentials in the Kohn-Sham-Dirac Hamiltonian to zero; (ii) the "Hartree-only" density profile, which is obtained by solving the Kohn-Sham-Dirac equations self-consistently with $V_{\rm xc}(\boldsymbol{r})=0$; and (iii) the "full" density profile, which includes both Hartree and exchange-correlation effects. The self-consistent calculations are iterated until the Kohn-Sham potential is converged to a relative precision of $\sim 10^{-3}$.

Electron-hole puddles, similar to those observed in Refs. 22 and 23, are evident in all these plots, although there are qualitative and quantitative differences between the noninteracting density profile and the ones that include electron-electron interactions. (The experimental observation that the spatial pattern of electron-hole bubbles is not correlated with the topography of the graphene sheets[23] is consistent with the inference[20,21] from conductivity-vs-carrier-density data that remote charges rather than sheet corrugations dominate disorder.) To begin with, we note how the inclusion of the Hartree term has the (expected) effect of reducing the amplitude of the spatial fluctuations of $\delta n(\boldsymbol{r})$ quite dramatically by ap-

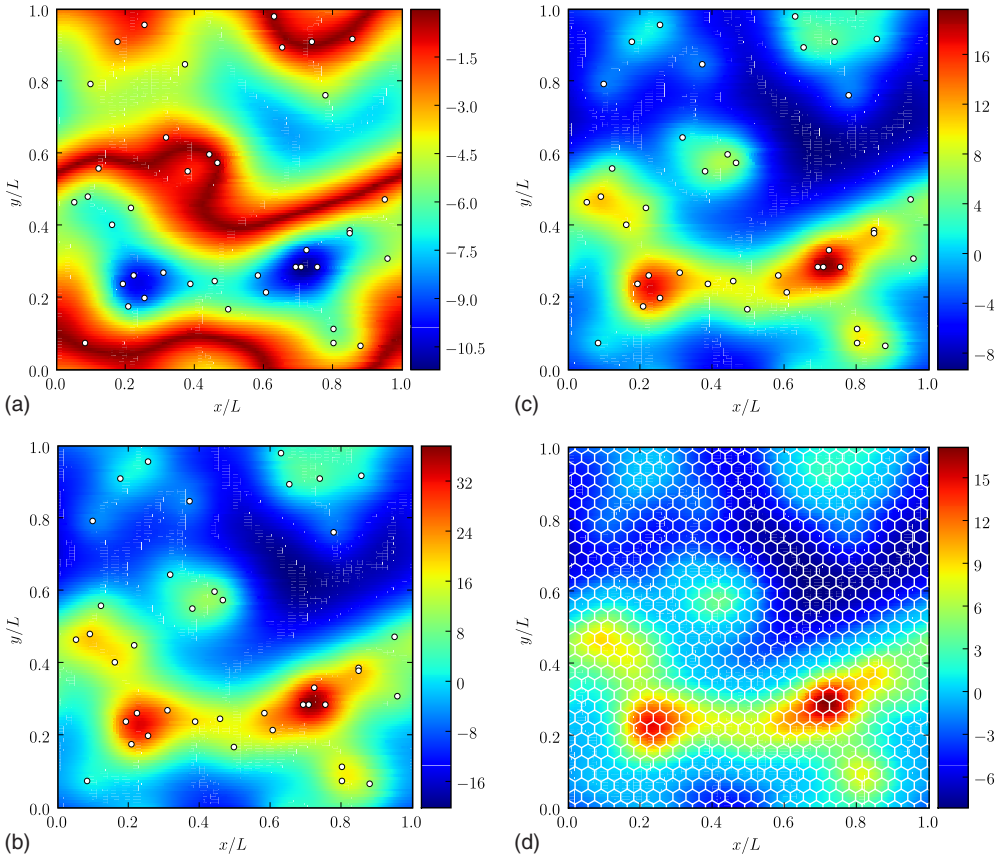

FIG. 2. (Color online) Top left panel: The plot of the external potential $V_{\rm ext}(\boldsymbol{r})$ (in units of $\hbar v/L$) as a function of x/L and y/L. The system parameters are $N_x=N_y=128$, $k_c=(2\pi/L)10$, $N_{\rm imp}=40$, $Z=+1$, $\alpha_{\rm ee}=0.5$, $\mathcal{Q}=0$, and $d/L=0.1$. The small circles represent the positions of the impurities for a particular realization of disorder. Top right panel: The color plot of the corresponding noninteracting ground-state density profile $\delta n(\boldsymbol{r})$ (in units of $1/L^2$) as a function of x/L and y/L. Bottom left panel: Hartree-only ground-state density profile. Bottom right panel: Same as in the bottom left panel but with the addition of the exchange and RPA correlation potentials. The honeycomb lattice is shown in this panel to illustrate the size of the simulation cell with respect to graphene's unit cell ($L^2=882\mathcal{A}_0$).

proximately a factor of 2 in these nonlinear screening calculations. It is interesting to compare this reduction factor with what would be expected in a linear screening approximation. Neutral graphene has the unusual property that its static dielectric function $\varepsilon(q)$ neither diverges as wave vector q goes to zero, as it would in a 2D metal, nor approaches 1, as it would in a 2D semiconductor. Instead

$$\varepsilon(q) = 1 - \frac{2\pi e^2}{\epsilon q}\widetilde{\chi}_{\rho\rho}(q) \tag{38}$$

approaches a constant because the polarization function $\widetilde{\chi}_{\rho\rho}(q)$ (or *proper* density-density response function[13]) has a nonanalytic linear dependence on q due to interband transitions with vanishing energy denominators. In the Hartree approximation [$\widetilde{\chi}_{\rho\rho}(q)\to\chi^{(0)}(q)$, where $\chi^{(0)}(q)$ is the noninteracting polarization function;[4] see Sec. 5.3.1 of Ref. 13 for more details],

$$\varepsilon(q) \to 1 + \frac{\pi}{8} g \alpha_{\rm ee} \sim 1.78 \tag{39}$$

for the value of $\alpha_{\rm ee}$ used in our calculations. When exchange and correlation corrections are included, $\varepsilon(q)$ increases by a small fraction, enhancing screening. The influence of interactions on the nonlinear screening calculations summarized in Fig. 2 is therefore (perhaps surprisingly) broadly consistent with expectations based on linear screening theory—even at a semiquantitative level. Qualitative nonlinear effects do however appear in some details, as we now explain.

In Fig. 3 we examine the induced carrier density in more detail by plotting $\delta n(\boldsymbol{r})$ as a function of x for a fixed value of y. Here we see clearly that $V_{\rm xc}(\boldsymbol{r})$ tends to cause the density to vary less rapidly in those spatial regions at which the carrier-density changes sign. The origin of this behavior in our calculations is that the exchange-correlation potential increases especially rapidly with density in these regions. This aspect of the induced density profile is similar to the behavior which would be produced by an energy gap of ~0.1 eV in the graphene bands (see Fig. 1). The rapid change in exchange-correlation potential with density alters the statistical distribution of density values in a disordered sample, as studied in some detail using a Thomas-Fermi approximation for the noninteracting kinetic-energy functional (and including local-density-approximation exchange) by Rossi and Das Sarma[8] in a recent paper. The Thomas-Fermi theory is formally based on a gradient expansion of the total-energy density (see, e.g., Sec. 7.3.1 of Ref. 13). When applied to

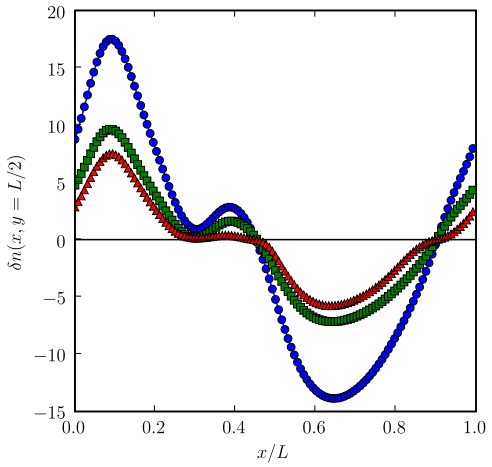

FIG. 3. (Color online) The one-dimensional plot of $\delta n(\boldsymbol{r})$ corresponding to the data in Fig. 2 as a function of x/L for $y/L=0.5$. The circles label the noninteracting result, the squares label the Hartree-only self-consistent result, and the triangles label the full self-consistent result.

graphene, assuming that the typical length scale for density variations in the 2D CEG is the inverse of the Thomas-Fermi screening wave vector $k_{\mathrm{TF}}=2\pi e^2\nu(\varepsilon_F)/\epsilon$ [here $\nu(\varepsilon_F)=g\varepsilon_F/(2\pi v^2)$ is the density of states at the Fermi energy], the Thomas-Fermi theory can be viewed as an expansion in powers of $k_{\mathrm{TF}}/k_F=g\alpha_{\mathrm{ee}}$. As emphasized by Fogler and co-workers,[9] this parameter is not small when the value used for α_{ee} is in the range of ~ 0.5 thought to be appropriate for graphene on SiO_2. In our approach we avoid a local-density approximation for the noninteracting kinetic-energy functional by solving microscopic Kohn-Sham-Dirac equations (this is the idea behind the Kohn-Sham mapping[11]). We cannot avoid the local-density approximation for the exchange-correlation potential however [Eq. (4)], and it must be acknowledged that this is a defect of our theory and one that is not easily remedied. The situation is similar to that in standard DFT applications, in which the local-density approximation is not rigorously valid on atomic length scales. It has nevertheless been possible to remedy defects of the local-density approximation in many circumstances by using modified functionals, such as, for example, generalized-gradient approximations, which are often semiphenomenological in character. Our expectation is that the LDA for exchange and correlation in graphene will improve accuracy compared to Thomas-Fermi approximation theories in which the band energy is also approximated using an LDA. In addition, it will likely prove possible to compensate for the main defects of the exchange-correlation LDA by using modified exchange-correlation energy functionals which are informed by comparisons between theory and experiment.

In Figs. 4 and 5 we report results similar to those presented in Figs. 2 and 3 but for a separate realization of the random charged impurity distribution and a smaller separation between the impurity plane and the graphene plane, $d=0.05L$. When the impurities are closer to the graphene plane, the role of the exchange-correlation potential seems to

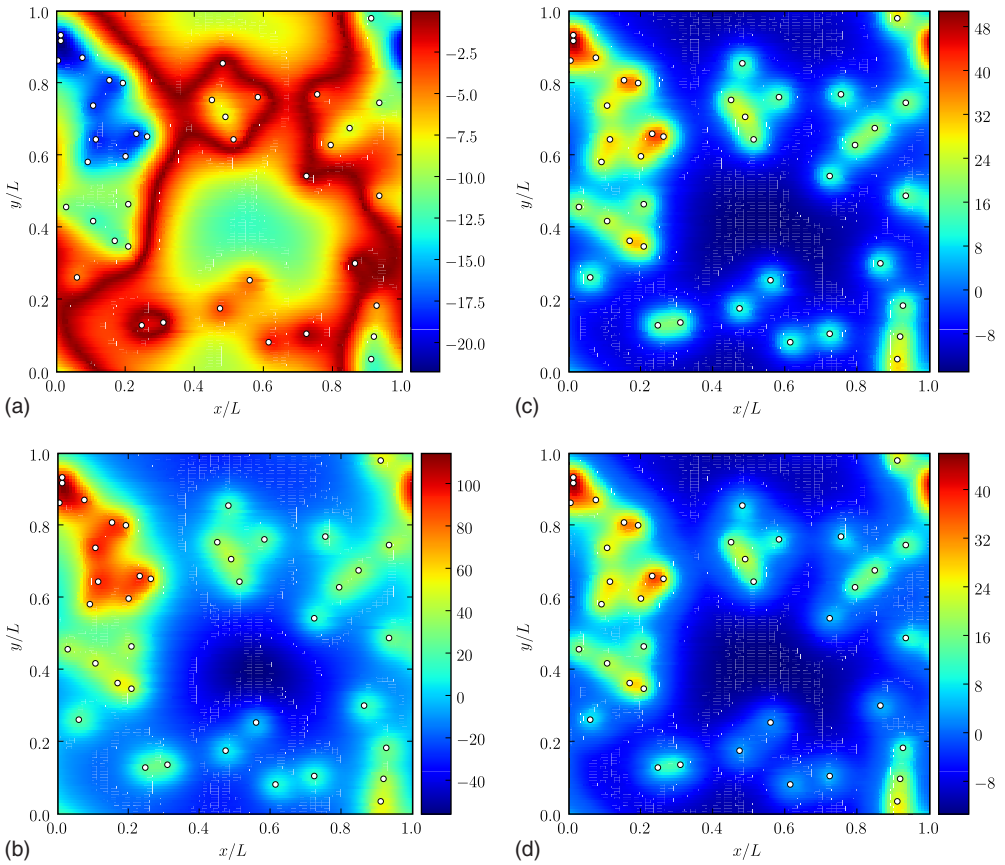

FIG. 4. (Color online) Same as in Fig. 2 but for a different distribution of charges and for $d/L=0.05$ instead of $d/L=0.1$.

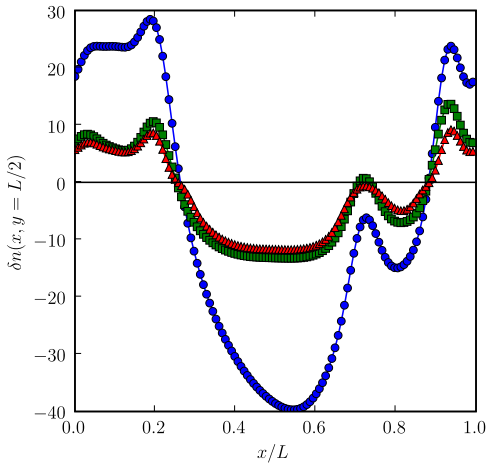

FIG. 5. (Color online) The one-dimensional plot of $\delta n(\boldsymbol{r})$ corresponding to the data in Fig. 4 as a function of x/L for $y/L=0.5$. The color coding is the same as in Fig. 3.

become less important. Conversely, for larger d exchange and correlation effects increase in importance. Because of the peculiar response of Dirac fermions, quite localized charge distributions can be induced by disorder potential features, even when those features are weak. Indeed we find that for large separations between the graphene and impurity planes, the Kohn-Sham-Dirac equations do not always converge, indicating the possible importance in some circumstances of correlation effects which cannot be captured by the KS LDA theory.

Finally in Figs. 6 and 7 we illustrate the dependence of $\delta n(\boldsymbol{r})$ on $\mathcal{Q}$, i.e., on gate potentials which move the average density away from the Dirac point. Because of the unavoidable presence of external charges in any graphene sheet environment, this is actually the generic case. Special neutral sheet properties, such as those referred to below in the single-impurity case, will be difficult to realize experimentally. Figure 6 shows the external potential created by a particular distribution of $N_{\mathrm{imp}}=40$ random charges, different again from the distributions used in producing Figs. 2–4, and the corresponding ground-state density profile $\delta n(\boldsymbol{r})$ calculated for $\mathcal{Q}=0$. The data in Fig. 6 refer to a system with square size $L^2=1922\mathcal{A}_0\sim 100$ nm^2. We then calculate $\delta n(\boldsymbol{r})$ for the *same* distribution of impurities but for $\mathcal{Q}=10$, 20, 30, and 40. The results of these simulations are shown and compared in Fig. 7. From this figure we clearly see that increasing the average density of the system increases the amplitude of the density fluctuations substantially when electron-electron interactions are neglected (see top panel of Fig. 7). When electron-electron interactions are included (see bottom panel of Fig. 7), this effect still occurs but $\delta n(\boldsymbol{r})$ seems to saturate with increasing $\mathcal{Q}$. Of course, the carrier-density fluctuation decreases in a relative sense with increasing $\mathcal{Q}$.

We conclude this section by reporting results for the single-impurity case. The calculation of the density distribu-

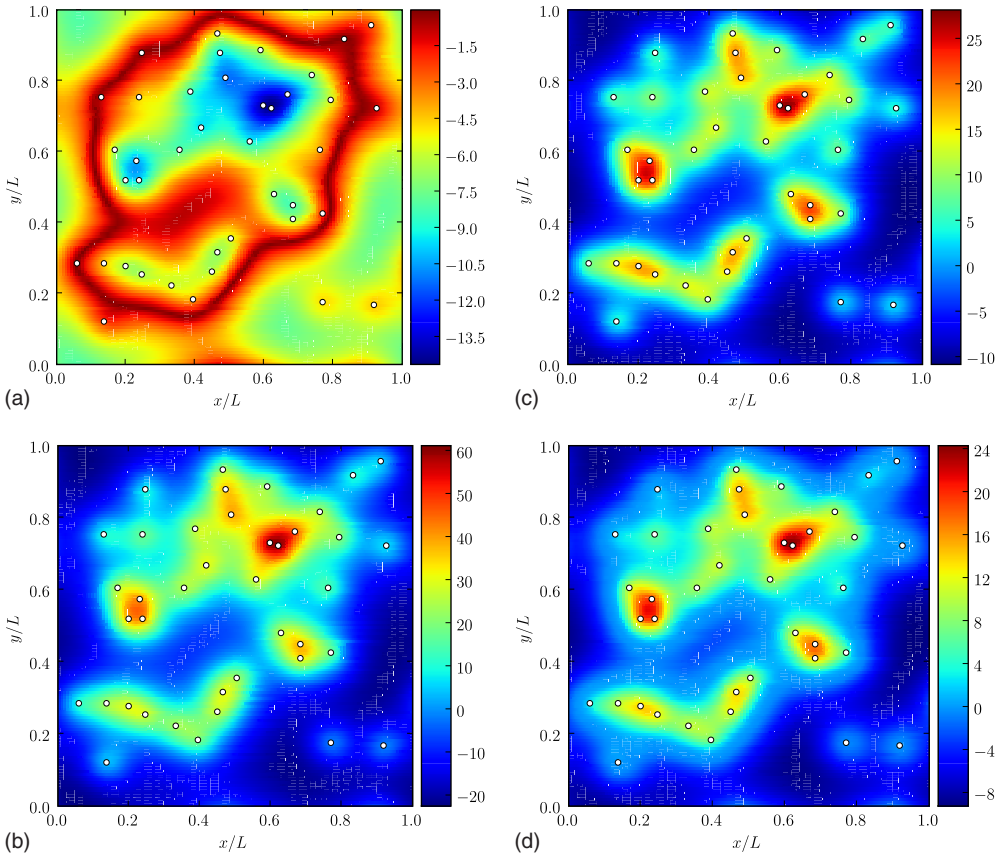

FIG. 6. (Color online) Same as in Figs. 2 and 4 but for a different distribution of impurities, $k_c=(2\pi/L)15$, and $d/L=0.07$.

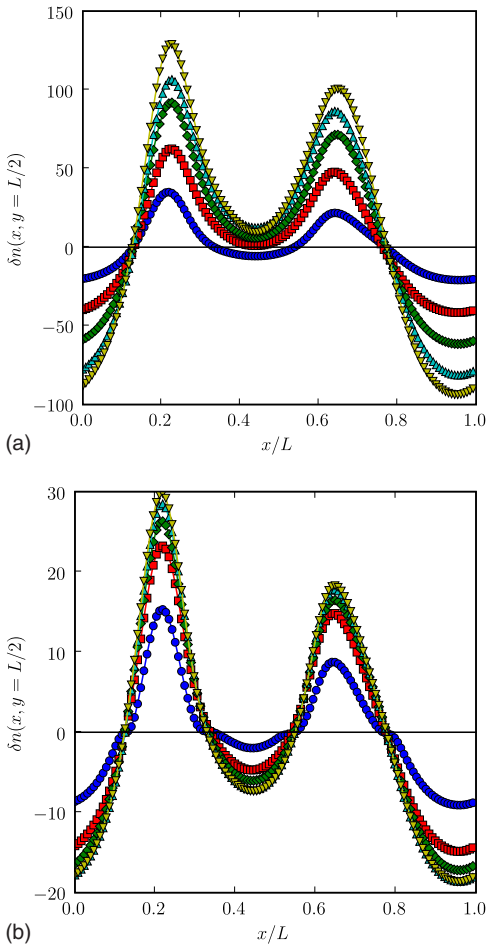

FIG. 7. (Color online) Illustrating the $\mathcal{Q}$ dependence of $\delta n(\boldsymbol{r})$. Top panel: The one-dimensional plot of the noninteracting density profile $\delta n(\boldsymbol{r})$ corresponding to the external potential in the top left panel of Fig. 6 as a function of x/L for $y/L=0.5$. The (blue) circles label the result for $\mathcal{Q}=0$, the (red) squares label the result for $\mathcal{Q}=10$, the (green) diamonds label the result for $\mathcal{Q}=20$, the (cyan) up triangles label the result for $\mathcal{Q}=30$, and the (yellow) down triangles label the result for $\mathcal{Q}=40$. Bottom panel: Same as in the top panel but for the full self-consistent density profile.

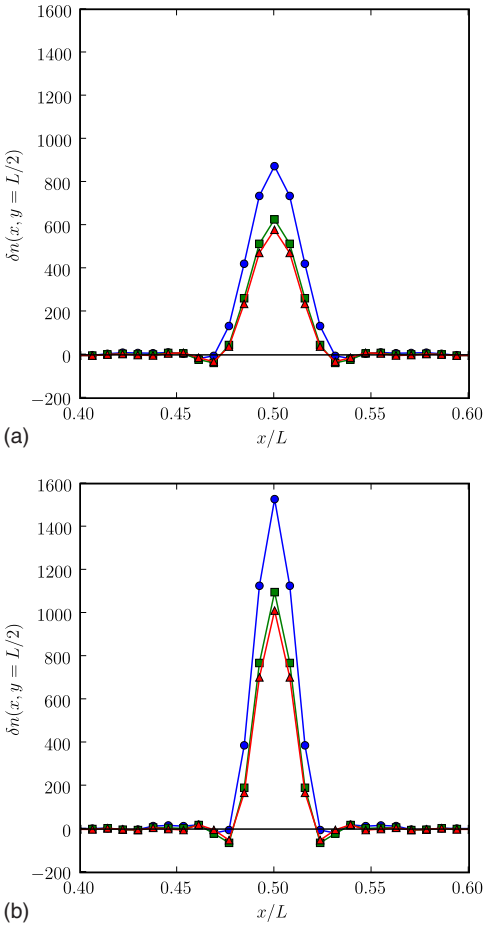

FIG. 8. (Color online) One-dimensional plots of $\delta n(\boldsymbol{r})$ as a function of x/L for $y/L=0.5$ for a single impurity with $Z=+1$ located at $x=y=L/2$. Here $d=0.0$ and $\alpha_{ee}=0.5$. Top panel: Numerical results for $k_c=(2\pi/L)15$. Bottom panel: Numerical results for $k_c=(2\pi/L)20$. The (blue) circles label the noninteracting result, the (green) squares label the self-consistent Hartree-only result, and the (red) triangles label the full self-consistent result.

tion of 2D noninteracting massless Dirac fermions in the presence of a single Coulombic impurity placed at the origin $\boldsymbol{R}_i=0$ of the graphene plane ($d=0$) has recently received a great deal of attention.[25–33] The analytical analysis reported in these works shows the existence of two different regimes: (i) a regime termed "subcritical," for $Z\alpha_{ee}<1/2$, in which the screening density $\delta n(\boldsymbol{r})$ is localized on the impurity, $\delta n(\boldsymbol{r})\propto\delta(\boldsymbol{r})$; and (ii) a regime termed "supercritical," for $Z\alpha_{ee}>1/2$, in which the screening density exhibits a power-law tail $\delta n(\boldsymbol{r})\sim 1/r^2$ at large distances. (A subregime termed "hypercritical," in which the induced charge density scales as $1/r^3$ for $\alpha_{ee}\sim 1$ and $Z\gg 1$, was identified within the supercritical regime in Ref. 31.) It is important to understand how these results are altered by the electron-electron interactions present in real graphene planes. The situation in graphene sheets is in this sense very different from standard semiconductor shallow-impurity problems, especially so when the Fermi level lies at the Dirac point. In the standard problem, it is a good approximation to truncate the Hamiltonian to a single band. Interactions then play no role since a single hole or single electron trapped by a charged impurity does not interact with itself. In graphene, on the other hand, both conduction and valence bands must be retained and the single-impurity problem is really a many-body problem.

The method used here to solve the Kohn-Sham-Dirac equations, which we project onto a plane-wave basis, is not optimized for the study of the single-impurity problem because it does not take advantage of its circular symmetry. Nonetheless, in Fig. 8 we present some numerical results for the density distribution of a 2D CEG in the presence of a single impurity placed at the center of the sample ($x=L/2$, $y=L/2$) and right on the graphene plane. In particular, we show a one-dimensional (1D) plot of $\delta n(\boldsymbol{r})$ as a function of x/L for $y/L=0.5$. These density profiles correspond to a $Z=+1$ impurity in a Dirac sea with $\alpha_{ee}=0.5$ and $\mathcal{Q}=0$. In the two simulation results reported in this figure, we have used $k_c=(2\pi/L)15$, which corresponds to an effective square size of $L^2=1922\mathcal{A}_0\sim 100$ nm^2, and $k_c=(2\pi/L)20$, which corresponds to an effective square size of $L^2=3362\mathcal{A}_0$

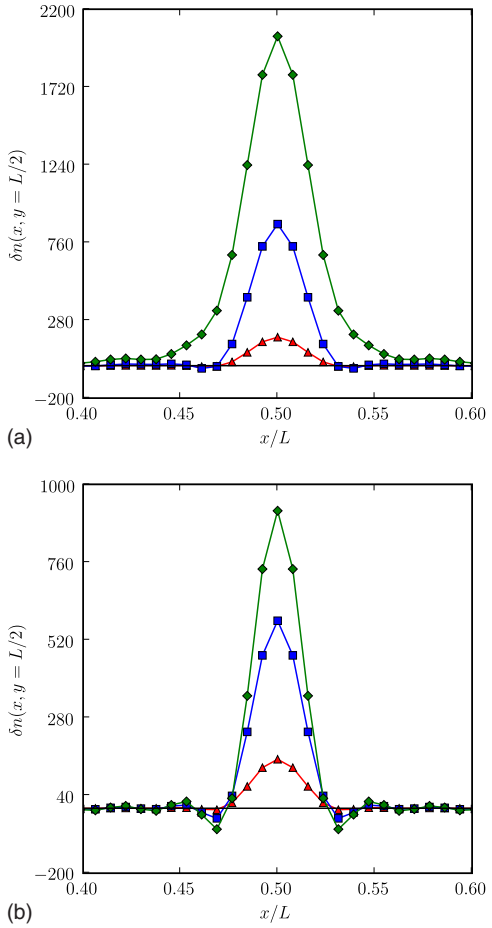

FIG. 9. (Color online) One-dimensional plots of $\delta n(\boldsymbol{r})$ as a function of x/L for $y/L=0.5$ for one impurity with $Z=+1$ located at $x=y=L/2$. Here $d=0.0$ and $k_c=(2\pi/L)15$. Top panel: Noninteracting results. Bottom panel: Full results. In each panel the (red) triangles label the results for $\alpha_{ee}=0.1$, the (blue) squares label the results for $\alpha_{ee}=0.5$, while the (green) diamonds label the results for $\alpha_{ee}=1.0$.

~ 175 nm^2. Comparing the results in the top $[k_c=(2\pi/L)15]$ and bottom $[k_c=(2\pi/L)20]$ panels, we can clearly see how they are compatible with a completely localized screening density with a δ-function shape, the finite width of $\delta n(\boldsymbol{r})$ being solely due to our momentum-space cutoff.

Finally, in Fig. 9 we show how $\delta n(\boldsymbol{r})$ behaves quite differently in the two cases $\alpha_{ee}=0.1$ and $\alpha_{ee}=1.0$. Indeed, the noninteracting density seems to possess a long-range tail for $\alpha_{ee}=1.0$. When electron-electron interactions are taken into account though, it seems that the behaviors of $\delta n(\boldsymbol{r})$ are quite similar in both cases. This is in agreement with the findings in Ref. 33 in which the authors showed that when electron-electron interactions are taken into account at the Hartree level, a $Z=+1$ impurity always remains in the subcritical regime.

V. DISCUSSION

When intervalley scattering is weak, doped and gated graphene sheets can be described using an envelope-function Hamiltonian with a new sublattice-pseudospin degree of freedom, an ultrarelativistic massless Dirac free-fermion term, a pseudospin scalar disorder potential, and a nonrelativistic instantaneous Coulombic interaction term. There is considerable evidence from experiment that this simplified description of a honeycomb lattice of carbon atoms is usually a valid starting point for theories of those observables that depend solely on the electronic properties of π electrons near the graphene Dirac point. Although the use of this model simplifies the physics considerably, it still leaves us with a many-body problem without translational invariance, which we do not know how to solve.

A common strategy in piecing together the physics of disordered interacting-fermion problems is to solve models in which interactions are neglected, appealing perhaps to Fermi-liquid-theory concepts, and to solve problems in which disorder is neglected, hoping that it is sufficiently weak to be unimportant for some observations. We anticipate that this *divide and conquer* approach will often fail in graphene. With this motivation, we have presented in this paper a Kohn-Sham-Dirac density functional theory scheme for graphene sheets, which treats interactions and smooth inhomogeneous external potentials on equal footing. Although it is formally an exact solution of the graphene many-body problem, it relies in practice on approximate exchange-correlation functionals.

The best approximation available for the graphene problem at present is the LDA for the exchange-correlation potential. In this paper we have provided convenient parametrizations of the exchange and correlation energies of uniform-density graphene systems based on random-phase-approximation many-body calculations. These results can be used to take account not only of density variations in a disordered graphene sheet but also of changes in the sheets' dielectric environment, which alters the coupling constant which appears in the Dirac model for graphene.

We believe that the exchange and correlation effects captured by our DFT theory will be important for many qualitative aspects of graphene electronic structure. In graphene the dependence of the LDA exchange-correlation potential on density is opposite to that of normal 2D or three-dimensional (3D) electron systems. As explained in detail in Ref. 5, the origin of this behavior is in the interplay between Dirac-model free-fermion pseudospin chirality and Coulomb interactions. When the carrier density is zero in a graphene sheet, the pseudospin-chirality polarization is maximized and this leads to lower interaction energies.

It is important to contrast the DFT scheme outlined in this paper with normal microscopic 3D DFT applied to the carbon atoms of a graphene sheet. The fully microscopic DFT deals with all the carbon atom orbitals, including the sp^2 bonding and antibonding orbitals, which are away from the Fermi level and neglected in the Dirac model, and can be used for example to calculate phonons, lattice constants, the electron-phonon coupling,[34] and the role of local atomic defects in a graphene sheet from first principles. Microscopic DFT also provides an *ab initio* estimate of the massless Dirac velocity, which is a phenomenological parameter of the Dirac-model theory. All these issues cannot be addressed by our Kohn-Sham-Dirac LDA 2D scheme. The advantages of

using the present DFT scheme for some π-orbital properties of graphene sheets are made clear by observing that microscopic 3D DFT, in which the exchange-correlation potential is based on the properties of a uniform 3D electron gas, fails to capture the anomalous sign of the density derivative of graphene's exchange-correlation potential. From a microscopic point of view this anomalous sign is a combined consequence of the peculiarities of Dirac bands and nonlocal exchange and correlation effects captured by the uniform-density Dirac-model. From a more practical point of view, the scheme proposed in this work can be implemented in a much easier way than traditional microscopic 3D DFT and is computationally much less demanding. Finally, because it is designed to work with a continuum model, it can handle much larger area graphene sheets.

In this paper we have illustrated the properties of this DFT description of disordered graphene sheets by concentrating on the nonuniform carrier density. Although the Kohn-Sham orbitals which appear in this and other DFT schemes are formally justified *only* for the role they play in density and ground-state-energy calculations (due to the Hohenberg-Kohn theorem[11]), their physical significance is often interpreted more liberally by associating the Kohn-Sham eigenvalues with quasiparticle energies. This pragmatic approach can fail spectacularly, as it famously does in the estimation of common semiconductor band gaps, but is more often quite useful in interpreting the spectral properties of materials. In the case of π-orbital properties of disordered graphene sheets, scanning-tunneling microscopy (STM) local density of states and angle-resolved photoelectron spectroscopy (ARPES) and optical conductivity spectra require interpretation. In our view it will be useful to apply the present approach as one element of an effort to improve understanding of what these probes tell us about particular graphene sheets. The fact that the self-energy of uniform-density graphene sheets has a large dependence on wave vector relative to the Dirac point,[5] in addition to its dependence on wave vector and energy relative to the Fermi surface, may help justify taking this liberty with the DFT formalism.

Before concluding this section, we would like to comment on the possibility of generalizing the present scheme to graphene bilayers. This can be done starting either from the kinetic Hamiltonian of the four-band model[1] or from the kinetic Hamiltonian of the two-band model,[35] in which two high-energy bands are neglected. (For recent comments on the range of validity of the two-band model, see Ref. 36.) In the latter case one still uses a two-component pseudospin language and thus the generalization of the present DFT scheme is straightforward. The appropriate spinors are given by[35] $\Phi_\lambda(\boldsymbol{r})=[\varphi_\lambda^{(A1)}(\boldsymbol{r}),\varphi_\lambda^{(B2)}(\boldsymbol{r})]^T$, the two components describing the amplitudes of electron waves on nearest sites $A1$ and $B2$ belonging to two nonequivalent carbon sublattices A and B and two (Bernal stacked) graphene layers marked as 1 and 2. The matrix elements of the kinetic Hamiltonian between plane-wave states are given by $-[\boldsymbol{k}'^2/(2m^\star)]\boldsymbol{\sigma}\cdot\hat{\mathbf{n}}\delta_{\boldsymbol{k},\boldsymbol{k}'}$, where $m^\star=\gamma_1/(2v^2)$ and $\hat{\mathbf{n}}=[\cos(2\varphi_{\boldsymbol{k}'}),\sin(2\varphi_{\boldsymbol{k}'})]$ with γ_1 as the interlayer tunneling amplitude and $\varphi_{\boldsymbol{k}'}=\arctan(k_y'/k_x')$. The Kohn-Sham potential for graphene bilayers becomes a nontrivial matrix in pseudospin space. The matrix elements of the Hartree term, for example, are given by[37]

$$\langle \boldsymbol{k}|\Delta V_H^{(\mu\nu)}|\boldsymbol{k}'\rangle = \delta_{\mu,\nu}\sum_\kappa [V_+(|\boldsymbol{k}-\boldsymbol{k}'|) + V_-(|\boldsymbol{k}-\boldsymbol{k}'|)\sigma^z_{\nu\nu}\sigma^z_{\kappa\kappa}]\delta\tilde{n}^{(\kappa)}(\boldsymbol{k}-\boldsymbol{k}'), \tag{40}$$

where μ, ν, and κ are pseudospin labels, $V_\pm(q)=[V_S(q)\pm V_D(q)]/2$, with $V_S(q)=2\pi e^2/\epsilon q$ (intralayer Coulomb interactions) and $V_D(q)=2\pi e^2\exp(-qd)/\epsilon q$ (interlayer Coulomb interactions), d being the interlayer separation. The RPA exchange-correlation potential of a uniform 2D liquid of electrons in a graphene bilayer, which is necessary to build the LDA exchange-correlation potential, is however not available presently.

VI. CONCLUSIONS

In this work we have outlined a Kohn-Sham-Dirac density functional theory scheme for graphene sheets that treats slowly varying inhomogeneous external potentials and electron-electron interactions on equal footing. The theory has the advantage over more conventional *ab initio* density functional methods of accounting for the unusual property that the exchange-correlation contribution to chemical potential increases with carrier density in graphene.[4–6] In this respect, we have presented convenient parametrization formulas for the exchange and random-phase-approximation correlation energies. We have solved the Kohn-Sham-Dirac equations self-consistently for a model random potential describing charged pointlike impurities located close to the graphene plane. We have shown how the exchange-correlation potential flattens the carrier density in those spatial regions where the latter changes sign, tending to create spatial separation between electrons and holes as recently observed experimentally.[22,23] Finally, we have also mentioned other problems to which the theory outlined in this paper could be successfully applied and we have outlined its generalization to bilayers.

ACKNOWLEDGMENTS

We gratefully acknowledge useful discussions with Victor Brar, Misha Fogler, Kentaro Nomura, and Gaetano Senatore. M.P. acknowledges the kind hospitality of the Department of Physics of the University of Texas at Austin during the final stages of the preparation of this work. M.P. was supported by the CNR-INFM "Seed Projects." A.H.M. was supported by the Welch Foundation, the USARO, and SWAN-NRI. The figures were prepared with the open source SCIPY/NUMPY/MATPLOTLIB packages of the PYTHON programming language.

*m.polini@sns.it

[1] A. K. Geim and K. S. Novoselov, Nat. Mater. **6**, 183 (2007); A. H. Castro Neto, F. Guinea, N. M. R. Peres, K. S. Novoselov, and A. K. Geim, arXiv:0709.1163, Rev. Mod. Phys. (to be published).

[2] For a recent popular review, see A. K. Geim and A. H. MacDonald, Phys. Today **60**, 35 (2007).

[3] The term "Kohn-Sham-Dirac" has been used earlier in the context of relativistic density functional theory of solids [see, e.g., A. H. MacDonald and S. H. Vosko, J. Phys. C **12**, 2977 (1979); and P. Strange, *Relativistic Quantum Mechanics* (Cambridge University Press, Cambridge, England, 1998)] and might thus confuse the reader. We are using the same term here simply because the Kohn-Sham equations we present below have a term [see first term in Eq. (1)], which is formally identical to the kinetic Hamiltonian of massless Dirac fermions.

[4] Y. Barlas, T. Pereg-Barnea, M. Polini, R. Asgari, and A. H. MacDonald, Phys. Rev. Lett. **98**, 236601 (2007).

[5] M. Polini, R. Asgari, Y. Barlas, T. Pereg-Barnea, and A. H. MacDonald, Solid State Commun. **143**, 58 (2007); M. Polini, R. Asgari, G. Borghi, Y. Barlas, T. Pereg-Barnea, and A. H. MacDonald, Phys. Rev. B **77**, 081411(R) (2008); M. Polini, R. Asgari, and A. H. MacDonald (unpublished).

[6] E. H. Hwang and S. Das Sarma, Phys. Rev. B **75**, 205418 (2007); S. Das Sarma, E. H. Hwang, and W.-K. Tse, *ibid.* **75**, 121406(R) (2007); E. H. Hwang, Ben Yu-Kuang Hu, and S. Das Sarma, *ibid.* **76**, 115434 (2007); Phys. Rev. Lett. **99**, 226801 (2007).

[7] M. C. Lemme, T. J. Echtermeyer, M. Baus, and H. Kurz, IEEE Electron Device Lett. **28**, 282 (2007); B. Huard, J. A. Sulpizio, N. Stander, K. Todd, B. Yang, and D. Goldhaber-Gordon, Phys. Rev. Lett. **98**, 236803 (2007); B. Özyilmaz, P. Jarillo-Herrero, D. Efetov, D. A. Abanin, L. S. Levitov, and P. Kim, *ibid.* **99**, 166804 (2007); J. R. Williams, L. DiCarlo, and C. M. Marcus, Science **317**, 638 (2007).

[8] E. Rossi and S. Das Sarma, arXiv:0803.0963 (unpublished).

[9] L. M. Zhang and M. M. Fogler, Phys. Rev. Lett. **100**, 116804 (2008); M. M. Fogler, D. S. Novikov, L. I. Glazman, and B. I. Shklovskii, Phys. Rev. B **77**, 075420 (2008).

[10] See, for example, P. Y. Yu and M. Cardona, *Fundamentals of Semiconductors* (Springer-Verlag, Berlin, 1999).

[11] P. Hohenberg and W. Kohn, Phys. Rev. **136**, B864 (1964); W. Kohn and L. J. Sham, *ibid.* **140**, A1133 (1965).

[12] W. Kohn, Rev. Mod. Phys. **71**, 1253 (1999); R. M. Dreizler and E. K. U. Gross, *Density Functional Theory* (Springer, Berlin, 1990); *Density Functionals: Theory and Applications*, Springer Lecture Notes in Physics Vol. 500, edited by D. Joulbert (Springer, Berlin, 1998).

[13] G. F. Giuliani and G. Vignale, *Quantum Theory of the Electron Liquid* (Cambridge University Press, Cambridge, England, 2005).

[14] N. Tombros, S. Tanabe, A. Veligura, C. Jozsa, M. Popinciuc, H. T. Jonkman, and B. J. van Wees, Phys. Rev. Lett. **101**, 046601 (2008); C. Jozsa, M. Popinciuc, N. Tombros, H. T. Jonkman, and B. J. van Wees, *ibid.* **100**, 236603 (2008).

[15] A. R. Akhmerov, J. H. Bardarson, A. Rycerz, and C. W. J. Beenakker, Phys. Rev. B **77**, 205416 (2008); J. L. Garcia-Pomar, A. Cortijo, and M. Nieto-Vesperinas, Phys. Rev. Lett. **100**, 236801 (2008); Di Xiao, W. Yao, and Q. Niu, *ibid.* **99**, 236809 (2007); I. A. Luk'yanchuk and A. M. Bratkovsky, *ibid.* **100**, 176404 (2008).

[16] A. De Martino, L. Dell'Anna, and R. Egger, Phys. Rev. Lett. **98**, 066802 (2007).

[17] G. Vignale and M. Rasolt, Phys. Rev. Lett. **59**, 2360 (1987).

[18] C. Attaccalite, S. Moroni, P. Gori-Giorgi, and G. B. Bachelet, Phys. Rev. Lett. **88**, 256601 (2002); **91**, 109902(E) (2003).

[19] M. Frigo and S. G. Johnson, Proc. IEEE **93**, 216 (2005); see also http://www.fftw.org/

[20] K. Nomura and A. H. MacDonald, Phys. Rev. Lett. **96**, 256602 (2006).

[21] E. H. Hwang, S. Adam, and S. Das Sarma, Phys. Rev. Lett. **98**, 186806 (2007); S. Adam, E. H. Hwang, V. Galitski, and S. Das Sarma, Proc. Natl. Acad. Sci. U.S.A. **104**, 18392 (2007).

[22] J. Martin, N. Akerman, G. Ulbricht, T. Lohmann, J. H. Smet, K. von Klitzing, and A. Yacoby, Nat. Phys. **4**, 144 (2008).

[23] V. W. Brar, Y. Zhang, C. Girit, F. Wang, A. Zettl, and M. Crommie, Bull. Am. Phys. Soc. **53** (2), 443 (2008).

[24] K. Nomura and A. H. MacDonald, Phys. Rev. Lett. **98**, 076602 (2007).

[25] D. P. DiVincenzo and E. J. Mele, Phys. Rev. B **29**, 1685 (1984).

[26] A. Kolezhuk, S. Sachdev, R. R. Biswas, and P. Chen, Phys. Rev. B **74**, 165114 (2006).

[27] M. I. Katsnelson, Phys. Rev. B **74**, 201401(R) (2006).

[28] A. V. Shytov, M. I. Katsnelson, and L. S. Levitov, Phys. Rev. Lett. **99**, 236801 (2007).

[29] V. M. Pereira, J. Nilsson, and A. H. Castro Neto, Phys. Rev. Lett. **99**, 166802 (2007).

[30] R. R. Biswas, S. Sachdev, and D. T. Son, Phys. Rev. B **76**, 205122 (2007).

[31] M. M. Fogler, D. S. Novikov, and B. I. Shklovskii, Phys. Rev. B **76**, 233402 (2007).

[32] D. S. Novikov, Phys. Rev. B **76**, 245435 (2007).

[33] I. S. Terekhov, A. I. Milstein, V. N. Kotov, and O. P. Sushkov, Phys. Rev. Lett. **100**, 076803 (2008).

[34] C.-H. Park, F. Giustino, M. L. Cohen, and S. G. Louie, Phys. Rev. Lett. **99**, 086804 (2007); M. Calandra and F. Mauri, Phys. Rev. B **76**, 205411 (2007); see, however, D. M. Basko and I. L. Aleiner, *ibid.* **77**, 041409(R) (2008).

[35] E. McCann and V. I. Fal'ko, Phys. Rev. Lett. **96**, 086805 (2006); K. S. Novoselov, E. McCann, S. V. Morozov, V. I. Fal'ko, M. I. Katsnelson, U. Zeitler, D. Jiang, F. Schedin, and A. K. Geim, Nat. Phys. **2**, 177 (2006).

[36] S. V. Kusminskiy, J. Nilsson, D. K. Campbell, and A. H. Castro Neto, Phys. Rev. Lett. **100**, 106805 (2008).

[37] H. Min, G. Borghi, M. Polini, and A. H. MacDonald, Phys. Rev. B **77**, 041407(R) (2008).